

## Facilitating *in vivo* tumor localization by principal component analysis based on dynamic fluorescence molecular imaging

Yang Gao  
Maomao Chen  
Junyu Wu  
Yuan Zhou  
Chuangjian Cai  
Daliang Wang  
Jianwen Luo

# Facilitating *in vivo* tumor localization by principal component analysis based on dynamic fluorescence molecular imaging

Yang Gao,<sup>a</sup> Maomao Chen,<sup>a</sup> Junyu Wu,<sup>b</sup> Yuan Zhou,<sup>a</sup> Chuangjian Cai,<sup>a</sup> Daliang Wang,<sup>b,\*</sup> and Jianwen Luo<sup>a,c,\*</sup>

<sup>a</sup>Tsinghua University, School of Medicine, Department of Biomedical Engineering, Beijing, China

<sup>b</sup>Tsinghua University, School of Medicine, Department of Basic Medical Sciences, Beijing, China

<sup>c</sup>Tsinghua University, Center for Biomedical Imaging Research, Beijing, China

**Abstract.** Fluorescence molecular imaging has been used to target tumors in mice with xenograft tumors. However, tumor imaging is largely distorted by the aggregation of fluorescent probes in the liver. A principal component analysis (PCA)-based strategy was applied on the *in vivo* dynamic fluorescence imaging results of three mice with xenograft tumors to facilitate tumor imaging, with the help of a tumor-specific fluorescent probe. Tumor-relevant features were extracted from the original images by PCA and represented by the principal component (PC) maps. The second principal component (PC2) map represented the tumor-related features, and the first principal component (PC1) map retained the original pharmacokinetic profiles, especially of the liver. The distribution patterns of the PC2 map of the tumor-bearing mice were in good agreement with the actual tumor location. The tumor-to-liver ratio and contrast-to-noise ratio were significantly higher on the PC2 map than on the original images, thus distinguishing the tumor from its nearby fluorescence noise of liver. The results suggest that the PC2 map could serve as a bioimaging marker to facilitate *in vivo* tumor localization, and dynamic fluorescence molecular imaging with PCA could be a valuable tool for future studies of *in vivo* tumor metabolism and progression. © 2017 Society of Photo-Optical Instrumentation Engineers (SPIE) [DOI: 10.1117/1.JBO.22.9.096010]

Keywords: dynamic fluorescence imaging; pharmacokinetics; principal component analysis; tumor localization.

Paper 170412R received Jun. 24, 2017; accepted for publication Aug. 29, 2017; published online Sep. 19, 2017.

## 1 Introduction

Molecular imaging uses specific molecules as the source of imaging contrast and visually represents biological events at the cellular and molecular level *in vivo*.<sup>1</sup> Fluorescence imaging has become a promising imaging modality as it provides non-radiative molecular imaging capability with advantages over other imaging modalities including decent detection sensitivity, specificity, safety, and instrumental cost-effectiveness.<sup>2</sup>

Autofluorescence and photon absorption in biological tissues remain at the minimum level in the near-infrared (NIR) wavelength range (700 to 900 nm), compared with those in the visible (350 to 700 nm) and infrared (above 900 nm) wavelength ranges. With the huge elimination of nonspecific fluorescence, using NIR fluorescent probes can improve the detection sensitivity.<sup>3,4</sup> Therefore, NIR fluorescence imaging serves as a promising tool for detecting specific biological molecules *in vivo*. Dynamic fluorescence imaging monitors the fluorescence signal of specific molecules over time and has been used to provide metabolic and pharmacokinetic information.<sup>5-8</sup>

Achieving *in vivo* cancer detection is of vast importance for diagnosis. To date, various types of molecular targets related to tumorigenesis and cancer progression such as integrin, metalloproteinase-2, and carbonic anhydrase IX have been used for tumor detection.<sup>9-14</sup> Epidermal growth factor receptor (EGFR, also known as HER-1) is another potentially effective molecular target. The EGFR signaling pathway plays a critical role in cell

signaling. The mutation of EGFR contributes to the proliferation, progression, and metabolism of tumor cells.<sup>15,16</sup> Numerous solid tumors over-express EGFR on the cell surface,<sup>17-19</sup> especially human lung carcinoma cell line A549,<sup>20-24</sup> making EGFR an eligible biomarker for *in vivo* cancer detection using fluorescence molecular imaging.

By combining target-binding molecules with fluorescent dyes, tumor-targeting fluorescent probes have been developed and employed to effectively facilitate cancer diagnosis. An NIR dye, IRDye CW800,<sup>25-31</sup> is coupled to recombinant human EGF, which binds specifically to EGFR, resulting in a specific EGFR-targeting fluorescent probe, EGF-IRDye. This probe has been shown to be capable of labeling tumor cells with EGFR-over-expression.<sup>32-37</sup> Once injected intravenously, this probe quickly reaches the liver, where it is processed and accumulated. Moreover, studies on the biodistribution of various tumor-targeting probes have shown that the unspecific probe aggregation in the liver is quite common.<sup>19,38-46</sup> Results of *ex vivo* tissue imaging<sup>40,44</sup> and *in vivo* imaging<sup>19,38,39</sup> have confirmed the high level of probe aggregation in the liver. Probe aggregation in the liver results in innegligible fluorescence background, which disrupts tumor imaging, especially when the tumors are located in the abdominal region.

To promote the specific targeting of tumor and distinguish tumor from surrounding tissues, various approaches have been put forward, including modifying the surface of the probe,<sup>38</sup> designing peptide probes sensitive to the tumor microenvironment,<sup>39</sup> using radiolabeled copper fibronectin-based imaging

\*Address all correspondence to: Jianwen Luo, E-mail: [luo\\_jianwen@tsinghua.edu.cn](mailto:luo_jianwen@tsinghua.edu.cn); Daliang Wang, E-mail: [wangdaliang@tsinghua.edu.cn](mailto:wangdaliang@tsinghua.edu.cn)

agents,<sup>40</sup> using tyrosine kinase inhibitors,<sup>41–43</sup> blocking the expression of EGFR in the liver,<sup>44</sup> and using dual-tracer molecular imaging.<sup>47–49</sup>

However, these approaches have limitations. Chemical modification of the imaging probe not only requires more bench work, but also might affect the stability, toxicity, and optical characteristics of the probe. Using radiolabeled imaging agents reasonably increases its uptake in tumor, but it also yields high renal uptake and retention<sup>40</sup> as well as high radioactivity distributed throughout the whole animal.<sup>42</sup> The coadministration strategy requires extra agents such as tyrosine kinase inhibitors<sup>41</sup> and radiolabeled exogenous EGF,<sup>42</sup> which might cause undesired physiological side-effects such as agonism and antagonism.<sup>40</sup>

Tumors have unique pharmacokinetic characteristics compared with surrounding tissues. Detecting these characteristics might be helpful in detecting and localizing the tumor. However, these characteristics are submerged in the high-dimensional original data of dynamic fluorescence imaging. Thus, extracting features related to tumor pharmacokinetic profiles could be a potential strategy for tumor detection and localization.

Functioning as a feature extraction algorithm, principal component analysis (PCA) assesses the original data and detects new variables called principal components (PCs), which are linear combinations of the original data.<sup>50</sup> Our group has used PCA to facilitate dynamic fluorescence diffuse optical tomography,<sup>51,52</sup> accelerate fluorescence molecular imaging,<sup>53–55</sup> and separate fluorescent targets with different fluorophore concentrations.<sup>56</sup> PCA has also been applied on dynamic fluorescence image sequences to extract *in vivo* anatomical maps, locate internal organs,<sup>57</sup> distinguish arteries and veins,<sup>58</sup> pinpoint tumor with the help of carbon nanotubes,<sup>59</sup> and extract physiological features related to both vasculopathy<sup>60,61</sup> and rheumatoid arthritis.<sup>62</sup>

The fluorescence signal from the tumor region is usually submerged by noise in the abdominal region, largely due to the probe aggregation in the liver. PCA has been used to identify tumors and other organs based on the different kinetics of non-specific probes.<sup>59</sup> To our knowledge, there are no reports of using PCA to suppress the fluorescence noise resulting from the aggregation of tumor-specific probes in the liver. Herein, we develop a PCA-based strategy to decrease the influence of probe aggregation in the liver and to facilitate tumor localization by extracting the tumor-related spatiotemporal features from results of dynamic fluorescence imaging.

The aim of this work was to distinguish the tumor region from the noise elicited by probe aggregation in the liver and to facilitate tumor localization based on dynamic fluorescence imaging. PCA was applied on the fluorescence imaging results of tumor-bearing and control mice, and the physiological meanings of the extracted PC maps were examined.

Our study provides the basis for a new way to eliminate fluorescence noise emerging from fluorescent probe aggregation in the liver to distinguish the tumor region. The results constitute an initial step toward facilitating tumor detection using PCA on molecular imaging with the help of a tumor-specific fluorescent probe. This approach has the potential to serve as a diagnostic tool for tumor detection and localization.

## 2 Methods

### 2.1 Cell Culture

A549 cells (purchased from ATCC, Manassas, Virginia) were maintained in RPMI 1640 medium supplemented with 10%

fetal bovine serum and 1% penicillin–streptomycin at 37°C in a humidified incubator. Cells were collected by trypsinization and resuspended in a culture medium before injection.

### 2.2 Nude Mice Xenograft Model

$5 \times 10^6$  A549 cells were injected subcutaneously into the back of three BALB/c-nude mice (8-week-old, female). Dynamic fluorescence imaging experiments were carried out when the average tumor diameter reached  $\sim 8$  mm (measured by a caliper). Animal experiments were conducted with approval from the Ethics Committee of Tsinghua University.

### 2.3 In Vivo Fluorescence Imaging

The fluorescent probe used to detect EGFR expression was EGF conjugated IRDye 800CW (EGF-IRDye; LI-COR Biosciences, Lincoln, Nebraska). A home-made reflectance fluorescence imaging system<sup>6,8,63</sup> was utilized for dynamic fluorescence imaging. A 300-W Xeon lamp (MAX-302, Asahi Spectra, Torrance, California) was used as the excitation source. The excitation light was filtered through a  $770 \pm 6$  nm bandpass filter (XBPA770, Asahi Spectra, Torrance, California) before reaching the object at a power density of  $0.03$  mW/cm<sup>2</sup>. The emitted fluorescence was filtered through an  $800 \pm 10$  nm bandpass filter (FBH800-10 Premium Bandpass Filter, Thorlabs, Newton, New Jersey) and then detected by a  $512 \times 512$  pixel,  $-70^\circ\text{C}$  electron multiplying charge-coupled device (EMCCD) camera (iXon DU-897, Andor Technologies, Belfast, Northern Ireland, UK) coupled with a 35-mm f/1.6 lens (C3514-M, Pentax, Tokyo, Japan). Each pixel has a size of  $0.16 \times 0.16$  mm<sup>2</sup>.

Mice were anesthetized with isoflurane, placed onto the platform of the reflectance fluorescence imaging system, and injected intravenously with a bolus of 1 nmol EGF-IRDye dissolved in 0.15 ml 1× phosphate buffer saline (PBS) (HyClone, Logan, Utah). Dynamic fluorescence imaging was started immediately after the intravenous injection. However, due to the limitations of the experimental apparatus, there was a delay ( $\sim 20$  s) between the end of injection and the beginning of the fluorescence image acquisition. The same experimental procedure was followed for every experiment to keep the length of these delays close to each other among experiments. The beginning of the fluorescence image acquisition was set to time point zero. Fluorescence images were collected at the speed of 1.5 frames per second for 900 s with the binning of the EMCCD camera set as one. The position of the mouse was maintained through the whole process of imaging. A bright-field image was collected afterward as the reference.

### 2.4 Probe Localization Studies

Mice were anesthetized with isoflurane and injected intravenously with 1 nmol EGF-IRDye (as described above) or 1× PBS, 900 s prior to the organ harvest. Organs including tumor xenograft, liver, and muscle (from the left thigh) were collected after the mice were euthanized. Harvested organs were immediately immersed in 1× PBS and rinsed before being imaged.

### 2.5 Data Analysis

#### 2.5.1 Principal component analysis

Our PCA-based approach was developed based on the previously described method,<sup>60</sup> the schematic is shown in Fig. 1.

Fluorescence images affected by motion artifacts were removed prior to the analysis ( $\sim 5\%$  of all original images). Removed images were recovered by interpolation to maintain the continuity of original image series. High-frequency noise was suppressed by applying lowpass filters on the original fluorescence images. The mouse body region was selected on the bright-field image and set as the mask [Fig. 1(a)], which was applied to the fluorescence images to select mouse body area and remove noise from the surface of the animal-holding platform.

Each fluorescence image was denoted by a two-dimensional matrix with its element representing the fluorescence intensity at the corresponding location. Each image in the sequence of  $m$  frames was vectorized to a column vector  $I$ , which has a length of  $n = 512 \times 512 = 262,144$  as follows:

$$I_k = \begin{bmatrix} i_{k1} \\ i_{k2} \\ \vdots \\ i_{kn} \end{bmatrix}, \quad (1)$$

where  $i_{kn}$  is the fluorescence intensity of the  $n$ 'th pixel on the  $k$ 'th frame.

An input matrix  $S$  was formed by gathering and arranging those  $m$  column vectors according to the order of time as follows:

$$S = [I_1 \ I_2 \ \cdots \ I_m]. \quad (2)$$

Therefore, the whole spatiotemporal features were incorporated in the input matrix  $S$ . Each row of  $S$  represents the temporal variation of fluorescence intensity at a certain pixel. Each column of  $S$  corresponds to the fluorescence intensities of all the pixels at a specific time point. [Fig. 1(b)]. The covariance matrix  $C$  was calculated as

$$C = \frac{1}{n-1} \bar{S}^T \bar{S}, \quad (3)$$

where  $\bar{S}$  is the centered data of  $S$ , calculated by subtracting the mean value from each column of  $S$ , and  $n$  is the length of each

column, as in Eq. (1). The eigenvectors  $U$  and eigenvalues  $\lambda$  of matrix  $C$  were then calculated as

$$C = U^T \lambda U. \quad (4)$$

The PCs were extracted and ranked in order of their eigenvalues. The eigenvector that has the highest eigenvalue was chosen as the first principal vector. The eigenvector with the second highest eigenvalue was considered the second principal vector and so on. The energy of the first  $i$  PC was calculated as

$$p_i = \frac{\sum_{k=1}^i \lambda_k}{\sum_{k=1}^m \lambda_k}. \quad (5)$$

The first two PCs contributed more than 99% of the total energy ( $p_2 > 99\%$ ); therefore, the first two PCs were considered to preserve the original information and were kept for further analysis.

The original fluorescence image sequence  $S$  was projected onto the new linear space  $x_p$  expanded by the PCs so that key features of the original data could be extracted and stored in matrix  $F$  as follows:

$$F = SU. \quad (6)$$

Each column of  $F$  was rearranged into a distribution map of each PC (PC1 map, PC2 map, etc.).

### 2.5.2 Time-dependent pharmacokinetic curves

Two rectangular regions of interest (ROIs) with a size of  $15 \times 15$  pixels were selected on each fluorescence image to represent the fluorescence intensities of the tumor and liver. On each fluorescence image, the approximate location of the tumor region was determined according to the bright-field image; then, the tumor ROI was selected around the pixel with the maximum fluorescence intensity in the tumor region. As for the liver, since the high-frequency noise was removed, the ROI was selected around the pixel that had the maximum fluorescence intensity of the entire image. The fluorescence intensity of the ROI was calculated by averaging the intensities of all pixels in that ROI. The intensities of the ROIs in the liver and tumor

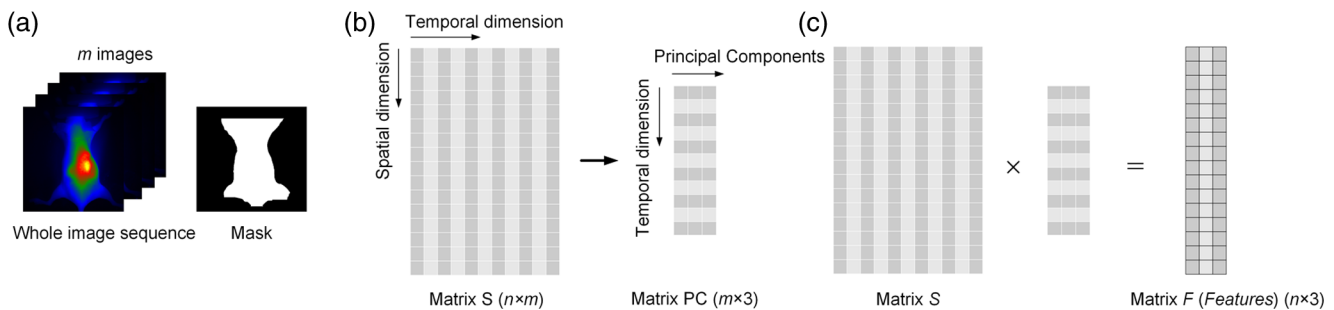


**Fig. 1** A schematic of PCA on dynamic fluorescence image data. (a) In the original sequence with  $m$  fluorescence images, a mask was applied to each image; thus, only the fluorescence intensities of the mouse body were taken into account. Each image was then vectorized into an  $n \times 1$  column vector  $I$  ( $n$  is the number of pixels in the mask). (b)  $m$  vectors were gathered to generate an  $n \times m$  matrix  $S$ .  $S$  contains all spatiotemporal information of the original image sequence. Eigenvectors and eigenvalues were calculated from  $C$ , which is the covariance matrix of  $S$ . The eigenvector with the highest eigenvalue was regarded as the first PC, and the eigenvector with the second highest eigenvalue was regarded as the second PC. Two PCs were kept for future analysis as they maintained more than 99% of total energy. (c) Features of the original data were extracted by calculating the inner product of  $S$  and PCs, and then these features were stored in the matrix  $F$ . Each column of  $F$  was rearranged to form a distribution map of corresponding PC, which represents feature of the original fluorescence image data.

were normalized base on the intensities at the first time point and then plotted against time, resulting in pharmacokinetic curves of these regions. It should be noted that, due to the aforementioned delay before fluorescence image acquisition, the liver and tumor region already exhibited fluorescence signals in the first fluorescence image, which was used later for normalization.

### 2.5.3 Tumor-to-liver ratio

The tumor-to-liver ratio is the ratio between the fluorescent probe uptake quantity in the tumor and liver.<sup>44,64</sup> In this study, it is defined as the ratio between the fluorescence intensities of the tumor and liver as follows:

$$r = \frac{FI_{\text{tumor}}}{FI_{\text{liver}}}, \quad (7)$$

where  $FI_{\text{tumor}}$  and  $FI_{\text{liver}}$  are the fluorescence intensities extracted from the ROIs selected in the tumor and liver, respectively. The tumor-to-liver ratio was used to evaluate the capability of distinguishing the tumor from the liver in the PC2 map.

### 2.5.4 Jaccard's similarity index

The tumor region was determined based on the bright-field image as the reference. The tumor location on the PC2 map was identified as the region with intensities higher than 70% of the maximum intensity of PC2. This threshold value was determined empirically. To quantify the similarity between the tumor locations on the PC2 map and on the bright-field image, the Jaccard's similarity index<sup>65</sup> was employed as an overlapping-based approach. The Jaccard's similarity index of two regions  $A$  and  $B$ ,  $J(A, B)$ , is defined as

$$J(A, B) = \frac{\text{card}(A \cap B)}{\text{card}(A \cup B)}, \quad (8)$$

where  $\text{card}(A \cap B)$  and  $\text{card}(A \cup B)$  are the cardinalities (i.e., numbers of elements) of  $A \cap B$  (the intersection of  $A$  and  $B$ ) and  $A \cup B$  (the union of  $A$  and  $B$ ), respectively. The Jaccard's similarity index ranges from 0 to 1, with 1 indicating a complete overlap of the two regions.

### 2.5.5 Contrast-to-noise ratio

The contrast-to-noise ratio (CNR) is defined according to Ref. 66 as follows:

$$\text{CNR} = \frac{\mu_S - \mu_B}{[\omega_S \sigma_S^2 + \omega_B \sigma_B^2]^{1/2}}, \quad (9)$$

where  $\mu_S$  is the mean intensity in the target region and  $\mu_B$  is the mean intensity in the background,  $\sigma_S$  and  $\sigma_B$  are the standard deviations of the intensities in the target region and the background, respectively, and  $\omega_S = \text{area}_S / (\text{area}_S + \text{area}_B)$  and  $\omega_B = \text{area}_B / (\text{area}_S + \text{area}_B)$  are the noise weights.  $\text{area}_S$  and  $\text{area}_B$  are the sizes of the target region and the background, respectively. The target region is the tumor region, which was determined based on the bright-field image. After the target region is excluded from the whole mouse body region, the rest of the mouse body region is determined as the background region.

### 2.5.6 Statistical analysis

Data were expressed as mean  $\pm$  standard deviation. Statistical differences were calculated by a two-tailed Student *t*-test. A  $p$  value  $< 0.05$  is considered statistically significant.

## 3 Results

### 3.1 Probe Accumulation in Liver and Tumor

To validate that the fluorescence signals were actually emitted from the fluorescent probe and to examine probe localization, the mice were injected with EGF-IRDye or 1 $\times$  PBS. Organs were harvested and imaged 15 min after the injection. A bright-field image was taken to show the harvested organs [Fig. 2(a), top]. Upon injection, the EGF-IRDye probe exhibited stronger emission in the tumor (a5) than in the muscle (a6). Neither the tumor (a2) nor muscle (a3) emitted strong fluorescence after PBS injection. Moreover, while the liver from the control group (a1) showed nearly nondetectable emission following probe injection, a stronger fluorescence signal was observed from the liver (a4) compared with the tumor (a5) after probe injection. Corresponding fluorescence intensity values were extracted from the images [Fig. 2(b)] to better visualize the fluorescence intensity difference between the tumor and the liver.

### 3.2 Time-Dependent EGF-IRDye Pharmacokinetic Characteristics

The pharmacokinetic features of EGF-IRDye in the mice with xenograft tumor are presented in Fig. 3. Dynamic fluorescence images at several time points were selected to represent the temporal sequence [Fig. 3(a)]. The tumor region was difficult to observe and distinguish from the strong fluorescent signal of the liver, which corresponded to the *ex vivo* results [Fig. 2]. ROIs were selected in the tumor and liver regions and labeled in red and cyanine colors, respectively [Fig. 3(b)]. The average fluorescence intensities in these ROIs were extracted and normalized according to the initial fluorescence intensities. Pharmacokinetic dynamics of the corresponding region were represented by time-solving curves, which exhibited the unique pharmacokinetic profiles of the tumor and liver. [Fig. 3(c)].

### 3.3 Distinctive Characteristics and Distribution Maps of Principal Components

The spatial distribution maps of the first two PCs were obtained by projecting the original dynamic fluorescence intensity data onto the principal vectors, as described in Sec. 2. Interestingly, the PC2 map exhibited a distinct pattern compared with the original fluorescence images in the xenograft mice group [Fig. 4(a)]. Strong intensities on the PC2 map were mainly located in the tumor region rather than in the liver; thus, the PC2 map visually distinguished the tumor region. The tumor-to-liver ratio on the PC2 map was significantly increased compared with that on the original fluorescence image [Fig. 4(b)]. The tumor areas were selected on the bright-field image and PC2 map, respectively [Fig. 4(c)], as described in Sec. 2, and then the location similarity of selected tumor areas was evaluated by the Jaccard's similarity index. The Jaccard's similarity indexes between the tumor regions on the PC2 map and those on bright-field image were 0.86, 0.70, and 0.71 for three mice injected with EGF-IRDye probe, respectively. The PC2 maps

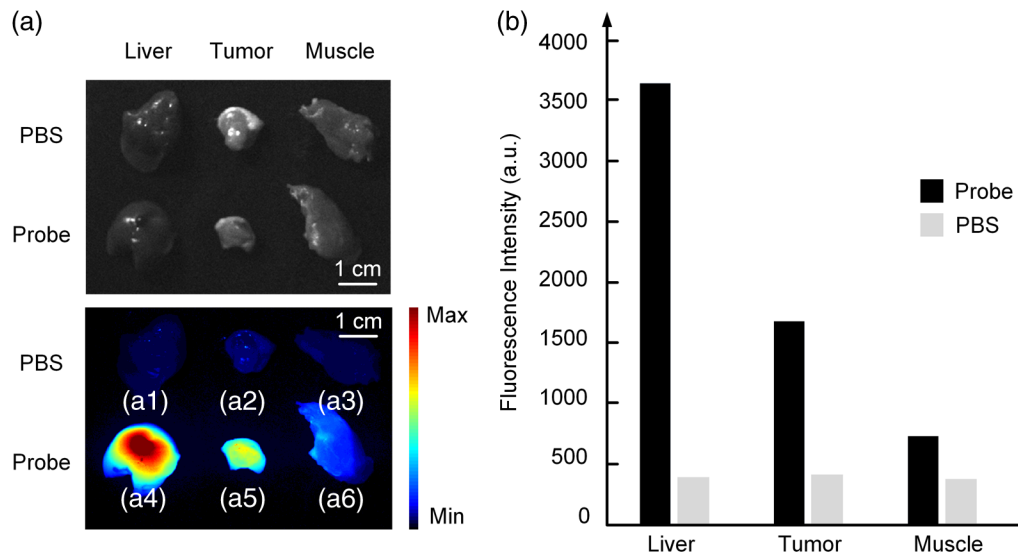


**Fig. 2** EGF-IRDye aggregated in the liver and tumor after intravenous injection. (a) Liver, tumor, and muscle were harvested from the mice injected with PBS (a1, a2, and a3, respectively) or EGF-IRDye (a4, a5, and a6, respectively). A bright-field image showed harvested organs (top). Following probe injection, the tumor showed significantly lower fluorescence intensity (a5) than the liver (a4), while they both exhibited higher fluorescence intensity compared with the muscle (a6). In the control group, the mice were injected with PBS, and all organs (a1, a2, and a3) emitted low level of fluorescence. (b) Fluorescence intensities of the liver, tumor, and muscle of the two groups.

exhibited higher tumor-to-liver ratios (2.34, 2.87, and 3.06) than the original fluorescence images (0.88, 0.67, and 0.64, respectively) [Fig. 4(d), left] and higher CNRs (4.55, 5.42, and 5.63 for three mice, respectively) than the original fluorescence image (2.56, 3.82, and 4.61, respectively) [Fig. 4(d), right].

Mice with tumor xenografts (the tumor-bearing groups) and healthy mice (the control groups) were injected with EGF-IRDye, and then the PC1 and PC2 maps of tumor-bearing groups and control groups were compared (Fig. 5). Notably, the PC2 map of normal controls showed an overall low level of fluorescence intensity, which was consistent with the fact

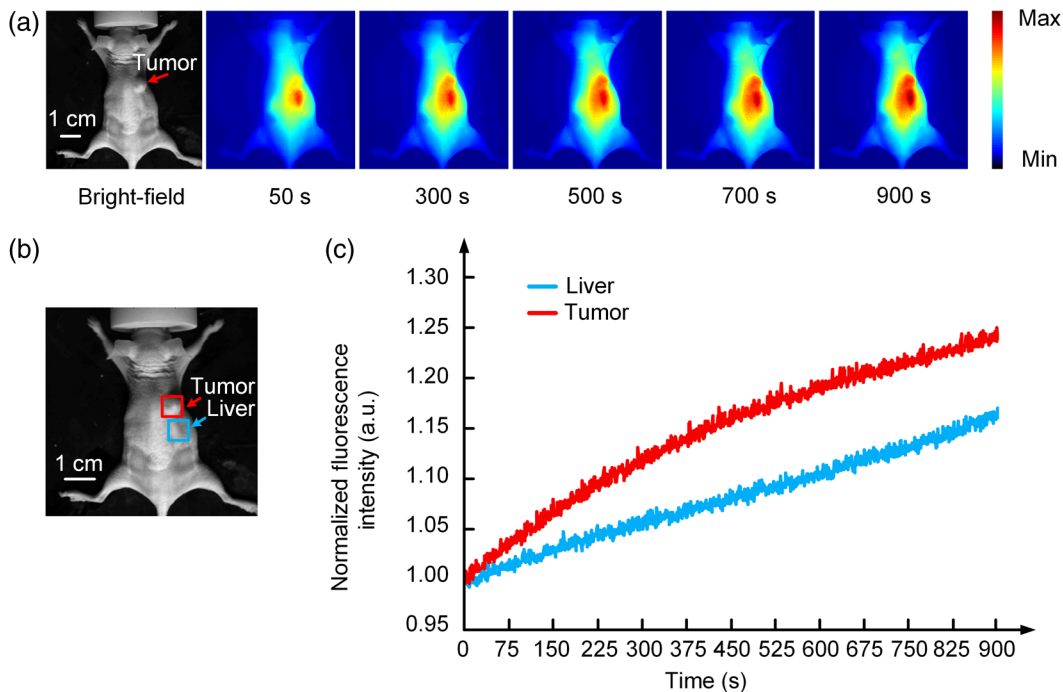


**Fig. 3** Original dynamic image sequences and pharmacokinetics. (a) Fluorescence images at different time points (50, 300, 500, 700, and 900 s after the first fluorescence image was collected). (b) ROIs were selected in the tumor and liver region, indicated by the square boxes of red and cyanine colors, respectively. The tumor location was indicated by the red arrow. (c) The normalized average fluorescence intensities of the liver and tumor were extracted from the original fluorescence images and plotted over time.

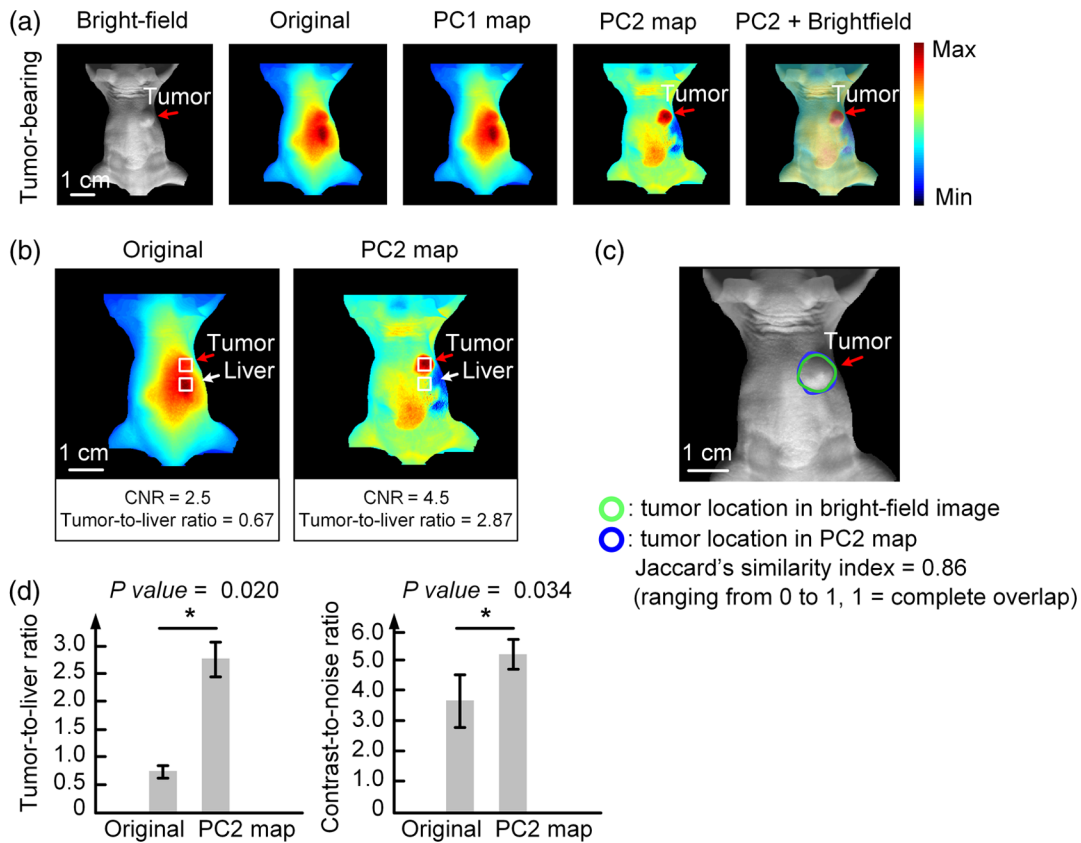


**Fig. 4** Distribution maps of the first two PCs in the tumor-bearing mice. (a) The bright-field image, original fluorescence image, PC1 map, and PC2 map. Note that the pattern of the PC2 map showed good accordance with the tumor location, as shown in the superposed image of the PC2 map and bright-field image. The tumor was indicated by the red arrow. (b) The ROIs used to calculate the CNR and tumor-to-liver ratio are indicated by the square boxes. The CNR (4.5 in the PC2 map and 2.5 in the original image) and the tumor-to-liver ratio (2.87 in the PC2 map and 0.67 in the original image) were labeled under the figure. (c) The tumor region was determined on the PC2 map (indicated by the blue curve) and bright-field image (indicated by the green curve), which served as the reference tumor location, as the tumor region could not be distinguished from the original fluorescence image. The Jaccard's similarity index between the tumor regions selected on the PC2 map and bright-field image was 0.86. (d) The tumor-to-liver ratio (left) and CNR (right) on the original fluorescence images and PC2 maps in the tumor-bearing group ( $n = 3$ ), respectively. The error bar indicated the standard deviation.

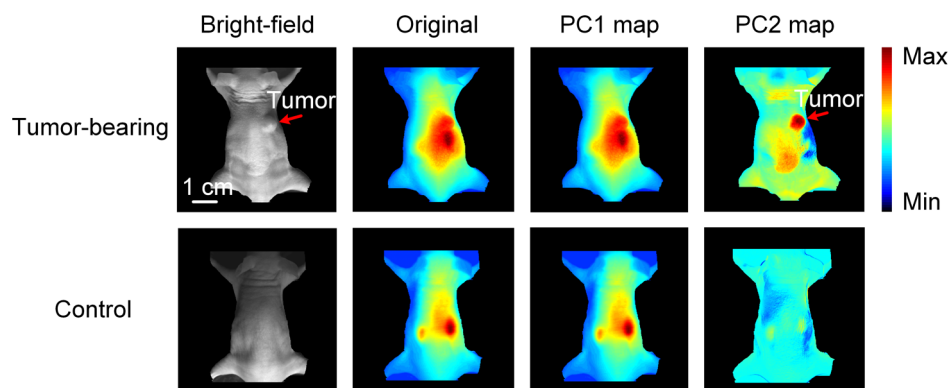


**Fig. 5** Distribution maps of PC1 and PC2 of the mice with tumor xenografts (the tumor-bearing groups) and healthy mice (the control groups) after they were injected with EGF-IRDye. The PC1 maps are in good accordance with the original fluorescence images, in both the tumor-bearing and control groups. The PC2 map of controls showed no prominent fluorescence signal.

that no tumor existed in the normal controls. The fluorescence intensity patterns of the PC1 map were in good accordance with those of the original fluorescence images in both the tumor-bearing mice and controls.

## 4 Discussion

The main goal of this study was to distinguish the tumor region from the noise elicited by probe aggregation in the liver and to facilitate tumor localization based on dynamic fluorescence imaging. In this study, distribution maps of PCs were extracted from dynamic fluorescence image data on the EGFR-expressing tumor xenograft model. The results show that the tumor region could be represented by PCs and distinguished from its nearby noise as the tumor-to-liver ratios were significantly increased.

Previous approaches to promote tumor localization include modifying the surface of probes,<sup>38</sup> designing microenvironment sensitive probes,<sup>39</sup> using radiolabeled imaging probes,<sup>40</sup> and using tyrosine kinase inhibitors and EGFR blockers.<sup>41–44</sup> Those approaches have helped the tumor targeting; however, they had limitations including extra bench work, toxicity of modified probes, and alteration of normal physiology.<sup>40,42</sup> PCA has been applied to help locate the tumor with the help of single-wall carbon nanotubes (SWNTs).<sup>59</sup> However, as a type of nonspecific probe, SWNTs accumulate in the tumor region mainly via the enhanced permeability and retention effect, rather than specific binding. In our study, the fluorescent probe could specifically bind to the surface of tumor cells, which enhances its accumulation in the tumor region. Our work attempted to facilitate tumor targeting by mathematically extracting the physiological features from the fluorescence image sequences with the help of the tumor-specific fluorescent probe. Moreover, our approach did not require extra modification of the imaging procedure. Notably, our strategy selected 900 s as the time for fluorescence image acquisition based on the considerations of promoting sufficient differences between probe kinetics of tumor and liver, as well as reducing the noise in the liver region on the PC2 map.

Unique pharmacokinetic characteristics of different regions [Fig. 3(b)] are the foundation of PCA in our study. Through PCA, the original high-dimensional fluorescence data were converted to low-dimensional data, and the important biological features were retained. These features could be potentially identified and represented by the PC maps.

Seo et al. have utilized PCA for vasculopathy diagnosis.<sup>60</sup> They found that the PC2 map was capable of representing vascular parameters and its dispersion showed a reverse pattern in diabetic patients and controls. We have adopted a similar strategy and acquired the tumor-related biological information directly from the PC maps. Our work used PCA with a tumor-specific fluorescent probe to facilitate the tumor detection with dynamic fluorescence imaging. Notably, our approach required only one kind of fluorescent probe and one emission wavelength to distinguish the tumor region from fluorescence noise in the abdominal region.

In the original fluorescence images, the tumor and the liver regions were joined with each other; thus, the tumor cannot be identified [Fig. 4(a)]. As the results show, the tumor was clearly indicated on the PC2 map, and these results suggested that our approach could facilitate tumor localization from two aspects. The first is the ability to distinguish the fluorescence signal of the tumor area from its nearby fluorescence noise (mainly from the liver). This could be validated by the increased

tumor-to-liver ratio and contrast-to-noise ratio of the PC2 map compared with the original image. The second aspect is the accuracy of tumor localization. By far, there is no “gold standard” for identifying the tumor location on the mouse xenograft model. The bright-field image directly presents the location of the subcutaneous tumor. Therefore, it was chosen as the reference for the tumor location. Herein, the Jaccard’s similarity index<sup>62</sup> was used to measure the location similarity of the tumor area determined by the PC2 map and the tumor area determined by the bright-field image. The Jaccard’s similarity index results (0.86, 0.70, and 0.71 for three mice, respectively) suggested that the tumor area identified by the PC2 map overlapped closely with the reference tumor location. Based on these findings, the PC2 map appeared to provide the information relevant to the tumor location. The overall original pharmacokinetic characteristics were visually represented in the PC1 map, and the PC2 map of the controls showed no prominent fluorescence signal (Fig. 5).

A number of limitations might have influenced the results. The first is the noise in the abdominal region on the PC2 map. This could be attributed to motion artifacts during the imaging process caused by respiration, although data affected by obvious artifacts had been removed prior to the analysis, as described in Sec. 2. The second limitation is the limited stage of tumor. In this study, experiments were conducted after the tumor sizes met certain preestablished criteria. Tumor vasculature rapidly changes during tumor development, and the vasculature affects the probe distribution. Tumors at different stages need to be examined to determine the exact stage when the tumor reaches maturity and exhibits pharmacokinetic characteristics that are distinct enough for the PCA strategy to detect. Third, the location of the tumor was determined directly on the bright-field images. This approach could be improved by labeling marker dots on the back skin of the nude mice along the margin of tumor xenografts and then using these markers for tumor localization on the bright-field images.

Furthermore, although the results are encouraging, the proposed method should be validated with a larger cohort size. Future work will also focus on further suppressing the motion artifacts elicited by respiration during the imaging process to reduce the noise level in the PC maps. Moreover, we intend to examine tumors of different stages to further evaluate the targeting capability of our PCA-based approach. Finally, yet importantly, we need to develop quantitative measurements of tumor pharmacokinetic profiles to thoroughly understand the *in vivo* tumor metabolism.

The encouraging results of our experiments indicate that the noise resulting from probe aggregation in the liver can be largely reduced by our PCA-based approach. The distribution maps of tumor-related PCs, which were extracted from dynamic fluorescence image sequences, could distinguish the tumor area from the noise in the abdominal region and improve tumor investigation. The approach has implications for future studies of *in vivo* tumor metabolism and progression.

## Disclosures

The authors have no competing financial interests to disclose in this manuscript.

## Acknowledgments

This work was supported by the National Natural Science Foundation of China under Grant Nos. 81227901, 81271617,

61322101, and 61361160418 and the National Major Scientific Instrument and Equipment Development Project under Grant No. 2011YQ030114. We would like to thank Wei Liu from the Department of Biomedical Engineering, School of Medicine, Tsinghua University, for his help with the animal experiments.

## References

- R. Weissleder, "Molecular imaging in cancer," *Science* **312**(5777), 1168–1171 (2006).
- F. Liu et al., "Monitoring of tumor response to Au nanorod-indocyanine green conjugates mediated therapy with fluorescence imaging and positron emission tomography," *IEEE Trans. Multimedia* **15**(5), 1025–1030 (2013).
- J. V. Frangioni, "In vivo near-infrared fluorescence imaging," *Curr. Opin. Chem. Biol.* **7**(5), 626–634 (2003).
- S. A. Hilderbrand and R. Weissleder, "Near-infrared fluorescence: application to in vivo molecular imaging," *Curr. Opin. Chem. Biol.* **14**(1), 71–79 (2010).
- G. Zhang et al., "A direct method with structural priors for imaging pharmacokinetic parameters in dynamic fluorescence molecular tomography," *IEEE Trans. Biomed. Eng.* **61**(3), 986–990 (2014).
- W. Cai et al., "Effects of temperature on multiparametric evaluation of hindlimb ischemia with dynamic fluorescence imaging," *J. Biophotonics* **10**(6–7), 811–820 (2016).
- M. Chen et al., "Fast direct reconstruction strategy of dynamic fluorescence molecular tomography using graphics processing units," *J. Biomed. Opt.* **21**(6), 066010 (2016).
- H. Guang et al., "Multiparametric evaluation of hindlimb ischemia using time-series indocyanine green fluorescence imaging," *J. Biophotonics* **10**(3), 456–464 (2017).
- V. Ermolayev et al., "Early recognition of lung cancer by integrin targeted imaging in K-ras mouse model," *Int. J. Cancer* **137**(5), 1107–1118 (2015).
- W. H. Kil et al., "Anticancer effect of silibinin on the xenograft model using MDA-MB-468 breast cancer cells," *Ann. Surg. Treat. Res.* **87**(4), 167–173 (2014).
- E. C. Nakajima et al., "Quantifying metabolic heterogeneity in head and neck tumors in real time: 2-DG uptake is highest in hypoxic tumor regions," *PLoS One* **9**(8), e102452 (2014).
- F. Liu et al., "Monitoring of tumor response to cisplatin with simultaneous fluorescence and positron emission tomography: a feasibility study," *J. Biophotonics* **7**(11–12), 889–896 (2014).
- B. Zhang et al., "In vivo tomographic imaging of lung colonization of tumour in mouse with simultaneous fluorescence and x-ray CT," *J. Biophotonics* **7**(1–2), 110–116 (2014).
- X. Chen, P. S. Conti, and R. A. Moats, "Near-infrared fluorescence imaging of integrin  $\alpha$  in brain tumor xenografts," *Cancer Res.* **64**(21), 8009–8014 (2004).
- R. I. Nicholson, J. M. W. Gee, and M. E. Harper, "EGFR and cancer prognosis," *Eur. J. Cancer* **37**, 9–15 (2001).
- M. F. Press and H.-J. Lenz, "EGFR, HER2 and VEGF pathways," *Drugs* **67**(14), 2045–2075 (2007).
- E. E. Helman et al., "Optical imaging predicts tumor response to anti-EGFR therapy," *Cancer Bio. Ther.* **10**(2), 166–171 (2010).
- Q. Zhou et al., "In vivo photoacoustic tomography of EGFR overexpressed in hepatocellular carcinoma mouse xenograft," *Photoacoustics* **4**(2), 43–54 (2016).
- Y. Zhang et al., "In vivo tomographic imaging with fluorescence and MRI using tumor-targeted dual-labeled nanoparticles," *Int. J. Nanomed.* **9**, 33–41 (2014).
- R. J. Mallia et al., "Wide-field multiplexed imaging of EGFR-targeted cancers using topical application of NIR SERS nanoprobe," *Nanomedicine* **10**(1), 89–101 (2015).
- X. Ren et al., "Modification of cytokine-induced killer cells with chimeric antigen receptors (CARs) enhances antitumor immunity to epidermal growth factor receptor (EGFR)-positive malignancies," *Cancer Immunol. Immunother.* **64**(12), 1517–1529 (2015).
- Q. Qin et al., "miR-134 inhibits non-small cell lung cancer growth by targeting the epidermal growth factor receptor," *J. Cell. Mol. Med.* **20**(10), 1974–1983 (2016).
- N. Tang et al., "Anti-tumor activity of high-dose EGFR tyrosine kinase inhibitor and sequential docetaxel in wild type EGFR non-small cell lung cancer cell nude mouse xenografts," *Oncotarget* **8**(6), 9134–9143 (2017).
- K. Uchibori et al., "Brigatinib combined with anti-EGFR antibody overcomes osimertinib resistance in EGFR-mutated non-small-cell lung cancer," *Nat. Commun.* **8**, 14768 (2017).
- M. Arjaans et al., "Bevacizumab-induced normalization of blood vessels in tumors hampers antibody uptake," *Cancer Res.* **73**(11), 3347–3355 (2013).
- M. Kijanka et al., "Rapid optical imaging of human breast tumour xenografts using anti-HER2 VHHs site-directly conjugated to IRDye 800CW for image-guided surgery," *Eur. J. Nucl. Med. Mol. Imaging* **40**(11), 1718–1729 (2013).
- J. L. Kovar et al., "Characterization of IRDye 800CW chlorotoxin as a targeting agent for brain tumors," *Anal. Biochem.* **440**(2), 212–219 (2013).
- A. M. Weihs et al., "Shock wave treatment enhances cell proliferation and improves wound healing by ATP release-coupled extracellular signal-regulated kinase (ERK) activation," *J. Biol. Chem.* **289**(39), 27090–27104 (2014).
- A. G. Bharadwaj et al., "Spontaneous metastasis of prostate cancer is promoted by excess hyaluronan synthesis and processing," *Am. J. Pathol.* **174**(3), 1027–1036 (2009).
- M. Meincke et al., "Near-infrared molecular imaging of tumors via chemokine receptors CXCR4 and CXCR7," *Clin. Exp. Metastasis* **28**(8), 713–720 (2011).
- A. Torres et al., "In vitro and in vivo activity of miR-92a-locked nucleic acid (LNA)-inhibitor against endometrial cancer," *BMC Cancer* **16**(1), 822 (2016).
- K. E. Adams et al., "Comparison of visible and near-infrared wavelength-excitable fluorescent dyes for molecular imaging of cancer," *J. Biomed. Opt.* **12**(2), 024017 (2007).
- J. L. Kovar et al., "Purification method directly influences effectiveness of an epidermal growth factor-coupled targeting agent for noninvasive tumor detection in mice," *Anal. Biochem.* **361**(1), 47–54 (2007).
- S. L. Gibbs-Strauss et al., "Detecting epidermal growth factor receptor tumor activity in vivo during cetuximab therapy of murine gliomas," *Acad. Radiol.* **17**(1), 7–17 (2010).
- S. Keereweer et al., "Optical image-guided surgery—where do we stand?" *Mol. Imag. Biol.* **13**(2), 199–207 (2011).
- K. M. Tichauer et al., "Improved tumor contrast achieved by single time point dual-reporter fluorescence imaging," *J. Biomed. Opt.* **17**(6), 066001 (2012).
- B.-W. Xie et al., "Dual-wavelength imaging of tumor progression by activatable and targeting near-infrared fluorescent probes in a bioluminescent breast cancer model," *PLoS One* **7**(2), e31875 (2012).
- J. L. Vivero-Escoto, R. C. Huxford-Phillips, and W. Lin, "Silica-based nanoprobe for biomedical imaging and theranostic applications," *Chem. Soc. Rev.* **41**(7), 2673–2685 (2012).
- D. Weerakkody et al., "Family of pH (low) insertion peptides for tumor targeting," *Proc. Natl. Acad. Sci. U. S. A.* **110**(15), 5834–5839 (2013).
- B. J. Hackel, R. H. Kimura, and S. S. Gambhir, "Use of  $^{64}\text{Cu}$ -labeled fibronectin domain with EGFR-overexpressing tumor xenograft: molecular imaging," *Radiology* **263**(1), 179–188 (2012).
- A. A. Memon et al., "Positron emission tomography (PET) imaging with [ $^{11}\text{C}$ ]-labeled erlotinib: a micro-PET study on mice with lung tumor xenografts," *Cancer Res.* **69**(3), 873–878 (2009).
- M.-R. Zhang et al., "[ $^{11}\text{C}$ ]Gefitinib ([ $^{11}\text{C}$ ]Iressa): radiosynthesis, in vitro uptake, and in vivo imaging of intact murine fibrosarcoma," *Mol. Imag. Biol.* **12**(2), 181–191 (2010).
- H. Wang et al., "Assessment of  $^{11}\text{C}$ -labeled-4-N-(3-bromoanilino)-6, 7-dimethoxyquinazoline as a positron emission tomography agent to monitor epidermal growth factor receptor expression," *Cancer Sci.* **98**(9), 1413–1416 (2007).
- H. Kareem et al., "Blocking EGFR in the liver improves the tumor-to-liver uptake ratio of radiolabeled EGF," *Tumor Biol.* **31**(2), 79–87 (2010).
- V. Tolmachev et al., "Imaging of EGFR expression in murine xenografts using site-specifically labeled anti-EGFR  $^{111}\text{In}$ -DOTA- $Z_{\text{EGFR}:2377}$  antibody molecule: aspect of the injected tracer amount," *Eur. J. Nucl. Med. Mol. Imaging* **37**(3), 613–622 (2010).

46. A. Becker et al., "Receptor-targeted optical imaging of tumors with near-infrared fluorescent ligands," *Nat. Biotech.* **19**(4), 327–331 (2001).
47. K. M. Tichauer et al., "Microscopic lymph node tumor burden quantified by macroscopic dual-tracer molecular imaging," *Nat. Med.* **20**(11), 1348–1353 (2014).
48. K. M. Tichauer et al., "Quantitative *in vivo* cell-surface receptor imaging in oncology: kinetic modeling & paired-agent principles from nuclear medicine and optical imaging," *Phys. Med. Biol.* **60**(14), R239–R269 (2015).
49. Y. Wang et al., "Raman-encoded molecular imaging (REMI) with topically applied SERS nanoparticles for intraoperative guidance of lumpectomy," *Cancer Res.* **77**(16), 4506–4516 (2017).
50. M. Ringner, "What is principal component analysis?" *Nat. Biotech.* **26**(3), 303–304 (2008).
51. X. Liu et al., "Principal component analysis of dynamic fluorescence diffuse optical tomography images," *Opt. Express* **18**(6), 6300–6314 (2010).
52. X. Liu, F. Liu, and J. Bai, "A linear correction for principal component analysis of dynamic fluorescence diffuse optical tomography images," *IEEE Trans. Biomed. Eng.* **58**(6), 1602–1611 (2011).
53. L. Xin et al., "Principal component analysis of dynamic fluorescence tomography in measurement space," *Phys. Med. Biol.* **57**(9), 2727–2742 (2012).
54. X. Cao et al., "Accelerated image reconstruction in fluorescence molecular tomography using dimension reduction," *Biomed. Opt. Express* **4**(1), 1–14 (2013).
55. G. Zhang et al., "Acceleration of dynamic fluorescence molecular tomography with principal component analysis," *Biomed. Opt. Express* **6**(6), 2036–2055 (2015).
56. H. Pu et al., "Separating structures of different fluorophore concentrations by principal component analysis on multispectral excitation-resolved fluorescence tomography images," *Biomed. Opt. Express* **4**(10), 1829–1845 (2013).
57. E. M. C. Hillman and A. Moore, "All-optical anatomical co-registration for molecular imaging of small animals using dynamic contrast," *Nat. Photonics* **1**(9), 526–530 (2007).
58. O. T. Bruns et al., "Next-generation *in vivo* optical imaging with short-wave infrared quantum dots," *Nat. Biomed. Eng.* **1**, 0056 (2017).
59. J. T. Robinson et al., "*In vivo* fluorescence imaging in the second near-infrared window with long circulating carbon nanotubes capable of ultrahigh tumor uptake," *J. Am. Chem. Soc.* **134**(25), 10664–10669 (2012).
60. J. Seo et al., "Principal component analysis of dynamic fluorescence images for diagnosis of diabetic vasculopathy," *J. Biomed. Opt.* **21**(4), 046003 (2016).
61. J. Seo et al., "Principal component analysis of indocyanine green fluorescence dynamics for diagnosis of vascular diseases," *Proc. SPIE* **9313**, 93131C (2015).
62. P. Mohajerani et al., "Spatiotemporal analysis for indocyanine green-aided imaging of rheumatoid arthritis in hand joints," *J. Biomed. Opt.* **18**(9), 097004 (2013).
63. Y. Li et al., "Primed 3D injectable microniches enabling low-dosage cell therapy for critical limb ischemia," *Proc. Natl. Acad. Sci. U. S. A.* **111**(37), 13511–13516 (2014).
64. B. M. Smithers et al., "Positron emission tomography and pathological evidence of response to neoadjuvant therapy in adenocarcinoma of the esophagus," *Dis. Esophagus* **21**(2), 151–158 (2008).
65. M. Levandowsky and D. Winter, "Distance between sets," *Nature* **234**(5323), 34–35 (1971).
66. X. Song et al., "Automated region detection based on the contrast-to-noise ratio in near-infrared tomography," *Appl. Opt.* **43**(5), 1053–1062 (2004).

**Yang Gao** received his bachelor's degree in pharmaceutical sciences from Tsinghua University, Beijing, China, in 2014. He is currently a PhD candidate in the Department of Biomedical Engineering, Tsinghua University, Beijing, China. His research interest is dynamic fluorescence molecular imaging for small animal imaging.

**Maomao Chen** received his bachelor's degree and master's degree in biomedical engineering from Chongqing University, Chongqing, China, in 2006 and 2009, respectively. He is currently a PhD candidate in the Department of Biomedical Engineering, Tsinghua University, Beijing, China. His research interest is fluorescence molecular tomography for small animal imaging.

**Junyu Wu** received his bachelor's degree from the School of Life Sciences and Technology, Tongji University, Shanghai, China, in 2011. He is currently a PhD candidate at the School of Medicine, Tsinghua University, Beijing, China. His research interests are the epigenetic regulation and cell biology of cancer cells.

**Yuan Zhou** received his bachelor's degree in biomedical engineering from Beijing Jiaotong University, Beijing, China, in 2014. He is currently a PhD candidate in the Department of Biomedical Engineering, Tsinghua University, Beijing, China. His research interest is fluorescence molecular tomography for small animal imaging.

**Chuangjian Cai** received his bachelor's degree in biomedical engineering from Tsinghua University, Beijing, China, in 2015. Currently, he is a PhD student in the Department of Biomedical Engineering, Tsinghua University. His research interest is fluorescence molecular tomography for small animal imaging.

**Daliang Wang** is an associate professor at Tsinghua University. She was enrolled in Tsinghua University in 2008 and received the foundation support from the 973 program of the Ministry of Science and Technology of China in 2011 and the National Natural Science Foundation of China in 2014. Her research interest is epigenetic regulation of tumorigenesis. She has published more than 20 journal papers in *Journal of Cell Biology*, *Cell Research*, *Journal of Biological Chemistry*, and so on.

**Jianwen Luo** is a professor at Tsinghua University. He was enrolled in the Thousand Young Talents Program in 2012, received the Excellent Young Scientists Fund from the National Natural Science Foundation of China (NSFC) in 2013, and was supported by the Young Scientists Project of National Key R&D Program of China in 2016. His research interests include ultrasound elasticity imaging and fluorescence molecular imaging. He has published more than 110 journal papers and 50 conference papers.